



Applying A-PTV to RBC suspension flows

Ang Sun¹ · Till Werner¹ · Finn Knüppel² · Frank-Hendrik Wurm² · Benjamin Torner² · Jeanette Hussong¹

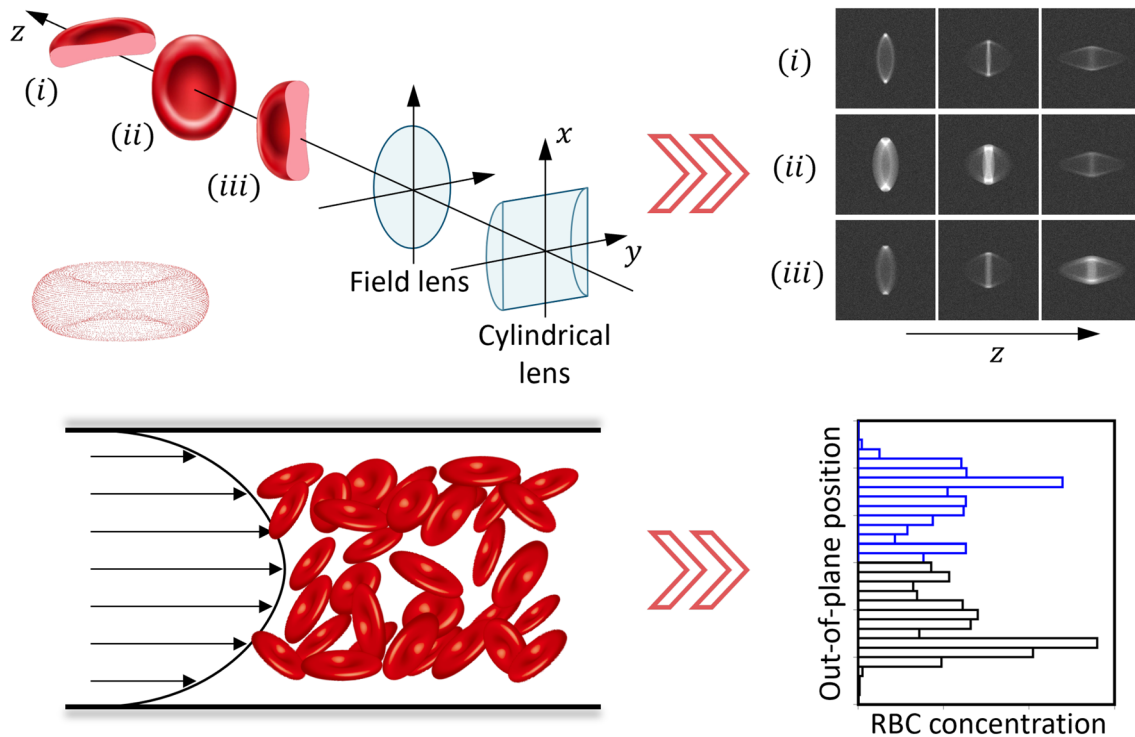
Received: 4 November 2024 / Revised: 17 January 2025 / Accepted: 19 January 2025
© The Author(s) 2025

Abstract

In strongly confined flow geometries, red blood cells migrate normal to the flow direction, thereby altering the flow rheology of blood. Direct optical measurements can help to gain an improved understanding of these migration processes. In the present study, we demonstrate that astigmatism particle tracking velocimetry is a suitable 3D-particle tracking method that allows to directly measure both 3D concentration and velocity distributions of red blood cells in a flow. Red blood cells assume a non-spherical shape; therefore, the influence of their orientation on the reconstruction of the out-of-plane particle position is evaluated through a ray tracing approach of synthetic, astigmatic images. While for noise-free images, the resulting absolute out-of-plane reconstruction error σ_z is small for different red blood cell orientations ($\sigma_z = 0.98 \mu\text{m}$), it triples for experimentally relevant signal-to-noise ratios ($\text{SNR} = 1.2$). Reconstruction errors are compared to those of spherical particles. Overall, both the red blood cell orientation and the increase in signal-to-noise ratio induce similar out-of-plane reconstruction error values. Experimental analyses are also performed using both a red blood cell suspension system and a refractive index-matched suspension system of identical volume fraction (1.5 %). Comparing results from the red blood cell suspension flow with those of the particulate suspension under identical parameters for volume fraction, particle Reynolds number, and bulk Reynolds number, a similarity in lateral migration behavior is observed under the given conditions. The results indicate that the absolute out-of-plane reconstruction error in the red blood cell suspension system ($\sigma_z = 4.50 \mu\text{m}$) is approximately 1.5 times larger compared to the refractive index-matched system.

Extended author information available on the last page of the article

Graphical Abstract



1 Introduction

Ventricular Assist Devices (VADs) are used in patients to mechanically pump blood in the body (Knüppel et al. 2023b). When excessive shear stress is created within a VAD, hemolysis may occur leading to rupture of red blood cells (RBCs) (Rodrigues et al. 2016; Fraser et al. 2012). Excessive hemolysis can result in hemolytic anemia (Ravichandran et al. 2014), which drastically reduces patients life expectation. In the VAD design process, hemolysis is typically estimated using numerical simulations. However, many models simplify blood as a single-phase fluid (Yu et al. 2017), ignoring the Fåhræus–Lindqvist effect, where RBCs migrate laterally away from vessel walls, forming a cell-free layer (CFL) near the wall. Such a CFL mainly consists of plasma (Fåhræus and Lindqvist 1931). Such variations in local RBC concentration induce variations in apparent local viscosity and therefore also affect the local shear stress distribution (Knüppel et al. 2023a, 2024).

To better understand the migration of RBCs in plasma, various experimental studies have been performed. High-speed imaging is commonly applied to track the motion of RBCs in blood flows (Bugliarello and Hayden 1963;

Tangelder et al. 1986; Japee et al. 2005). In addition, Kim et al. (2006) investigated the formation of a CFL in vitro by bright-field imaging. Classical video microscopy approaches are restricted to extract 2D velocities or concentration distributions that are averaged over the measurement-depth.

In stationary flows, 2D techniques may be combined with an out-of-plane scanning procedure to extract 3D information. Such measurement techniques are confocal μ PIV or μ PTV, which allow capturing 2D particle images in thin well-defined focal planes (Williams et al. 2010; Park et al. 2004). Lima et al. (2006, 2007, 2008, 2009) applied confocal μ PIV or μ PTV extensively to study the RBC behavior and corresponding velocity profiles for varying hematocrit levels at low Reynolds numbers ranging from 0.003 to 0.025. Confocal μ PIV or μ PTV, however, has strong limitations in temporal resolution due to the inherent in-plane scanning procedure. Therefore, it is restricted to low flow rates and particle image displacements.

Standard 2D μ PIV or μ PTV does allow for higher temporal resolution but suffers from large measurement volume depths that are typically larger than the particle diameter. This reduces the out-of-plane reconstruction accuracy of particle positions. As these scanning procedures allow to

access the three-dimensional, two-component (3D2C) particle or fluid velocity field, an additional reconstruction, based on a mass conservation approach, is necessary to access the out-of-plane velocity field.

Fully three-dimensional, three-component (3D3C) measurement techniques are therefore an attractive alternative. For example, digital holographic μ PIV enables the particle reconstruction in 3D space by evaluating the amplitude and phase information of an image. Satake et al. (2005, 2006) and Choi and Lee (2010) applied this method to measure particle positions and velocities in microchannel flows, achieving micron-level out-of-plane accuracy. However, the reconstruction process of digital holograms involves extensive image processing and computation to accurately extract particle positions. Moreover, the particle concentration is limited due to speckle noise (Discetti and Coletti 2018).

Defocusing techniques allow 3D3C measurements using a single camera by extracting the out-of-plane particle position and displacement by evaluating the particle image blur at each time step. As the particle image blur is a consequence of defocusing, information on the spacing between particle and focal plane can be extracted from it. Speidel et al. (2003) and Peterson et al. (2008) utilized this technique to achieve the out-of-plane position of fluorescent particles in suspensions with micron accuracy. Coutinho et al. (2023) applied the defocusing technique to platelet-sized fluorescent particles in a RBC suspension flows. They measured the positions as well as the velocities of the platelet-sized particles.

Stigmatic defocusing techniques bear an ambiguity of the out-of-plane position, as particles may be located above or below the focal plane. Such ambiguities can be avoided if astigmatic defocusing techniques are applied. In recent approaches astigmatic images are realized by adding a cylindrical lens in the optical path, creating two focus planes. 3D tracking approaches based on astigmatic imaging are referred to as astigmatic particle tracking velocimetry (A-PTV) (Kao and Verkman 1994). Particle images assume an elliptical shape whose aspect ratio and orientation varies with the particle's out-of-plane position, as shown in Fig. 1. The resulting astigmatic image is unambiguous, and the degree of astigmatism can be adjusted to the measurement task by the selection of the lens and its position. Kao and Verkman (1994) first used this technique to track single fluorescent particles in live cells. In recent years, A-PTV has been widely applied to measure the 3D positions and velocities of particles, achieving high out-of-plane reconstruction accuracies (Chen et al. 2009; Cierpka et al. 2010; Rossi et al. 2019). Since the 3D position can be directly obtained from single images, measurements with higher Reynolds numbers of $Re > 100$ are possible (Blahout et al. 2020). Brockmann and Hussong (2021); Brockmann et al. (2022) used refractive index matching

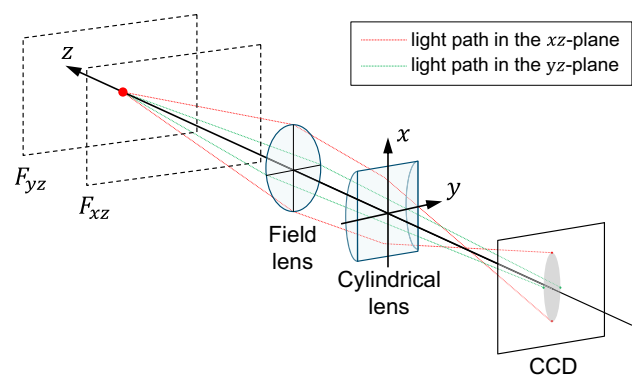


Fig. 1 Illustration of astigmatic imaging as used in A-PTV. Red light rays as indicated in the xz -plane have a focal point in front of the CCD. In contrast, light rays indicated here in green in the yz -plane remain unaffected by the cylindrical lens as there is no curvature in the y -direction. The corresponding focal point of those rays lie behind the CCD sensor. Overall, this results in an elliptical particle image on the CCD. F_{xz} and F_{yz} represent xz - and yz - focal planes of the optical system

to improve the optical accessibility in dense suspensions and successfully applied A-PTV to measure relative particle concentrations and velocities in monodisperse suspensions at up to 19.9 % volume fraction and polydisperse suspensions at 9.1 %. Traditionally, A-PTV is calibrated by quantifying the shape of the particle image and mapping it on a calibration curve (Cierpka et al. 2011). Later, Barnkob et al. (2015) proposed the general defocusing particle tracking (GDPT) approach. In this method a calibration image stack is assembled from particle images of known out-of-plane positions. Subsequently, the particle position of particles recorded during a flow measurement are reconstructed through a 2D cross-correlation procedure between measurement and calibration images. This approach significantly enhances the versatility of A-PTV and improves robustness against outliers and overlapping particles (Barnkob et al. 2015).

In the present study, A-PTV is employed for the first time to directly evaluate the 3D positions and in-plane velocities of RBCs. The work focuses on the analysis of out-of-plane position errors as they are a crucial quantity needed when evaluating RBC migration dynamics. Errors resulting from image noise and the orientation of RBCs are evaluated. This is achieved through the utilization of both synthetic and experimental data. Next, RBC velocities and distributions are measured through A-PTV in a suspension flow (1.5 %) at bulk Reynolds number of $Re_b = 150$. Such high Reynolds numbers are typically achieved in VAD gaps. The microchannel flow realized in the present study resembles key features of such a pressure driven VAD gap

flow. Experiments are conducted with a particulate suspension of stiff, spherical PMMA particles under identical dimensionless parameters to compare reconstruction errors to a suspension system of high optical quality as it is typically utilized for A-PTV measurements.

2 Methodology

To successfully perform 3D measurements on the migration dynamics of RBCs in a controlled environment, a portable, custom-built epifluorescence microscope was used. The measurement setup and the depicted flow geometry are explained in the following. Subsequently, the protocol for blood preparation and particulate blood-analogue fluid (pBAF) preparation are outlined. In a third step, the experimental execution steps are explained which include an in situ calibration followed by the actual flow experiments.

2.1 Experimental setup

Measurements are taken in a custom-built epifluorescence microscope. A schematic representation of the experimental setup is provided in Fig. 2. A double-pulse dual-cavity Nd:YAG laser (e) (*Litron Nano S 65-15 PIV*) is integrated into the system for illumination, and images are captured using a double-frame CCD camera (a) (*JAI CV-M2*) with a resolution of 1600 pixels \times 1200 pixels. A cylindrical lens (b) with a focal length of $f = 200$ mm is placed in front of the CCD camera. All images are magnified using an infinity-corrected objective (d) (*Nikon CFI60 TU Plan Epi ELWD*) with a magnification of $M = 20\times$

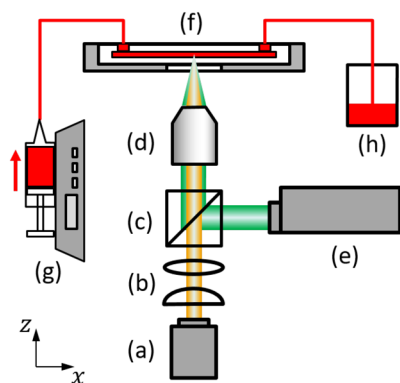


Fig. 2 Sketch of the experimental setup: **a** CCD camera, **b** cylindrical and field lens, **c** dichroic mirror with bandpass filters, **d** microscope objective, **e** Nd:YAG laser, **f** microchannel and channel holder, **g** syringe pump and syringe, **h** container

and a numerical aperture of $NA = 0.4$, resulting in a field of view of $0.55 \text{ mm} \times 0.55 \text{ mm}$ reaching a spatial resolution $0.46 \mu\text{m}/\text{pixel}$. A bandpass filter (c) with $575\text{--}625 \text{ nm}$ transmission wavelength is placed between the dichroic mirror and the camera to reduce unwanted signals, e.g., from laser reflections while the desired fluorescence signal of Rhodamine 6 G can pass to be recorded by the camera. The commercial software *DynamicStudio* (*Dantec Dynamics*) is used for image acquisition.

All measurements are taken in a straight rectangular microchannel, as shown in Fig. 3. This microchannel is fabricated from borosilicate glass by *Micronit Microfluidics BV* (*Enschede, NL*), with an isotropic wet etching technique. The microchannel has a length, width and height of $l \times w \times h = 40 \text{ mm} \times 2.33 \text{ mm} \times 150 \mu\text{m}$. The flow is driven by a syringe pump (g) (*HLL LA-800*) through the microchannel (f) and is then collected in a container (h), as shown in Fig. 2. The flow within this microchannel can be approximated as two-dimensional plane channel flow with an aspect ratio $w/h = 15.53$. As indicated in Fig. 3, all measurements are taken at the geometric center of the microchannel, located 20 mm downstream from the inlet in flow direction.

2.2 Sample preparation

Both suspensions with RBCs and spherical PMMA microparticles were prepared prior to the measurements. The RBC suspension was derived from healthy pigs. An ethylenediaminetetraacetic acid (EDTA) solution (1.5 mg/ml) was added immediately to the fresh blood as anticoagulant. Subsequently, multiple centrifugation and washing steps with phosphate-buffered saline (PBS) were performed. Replacing plasma with PBS as the carrier fluid for RBCs significantly enhances the optical accessibility of the suspension, which is advantageous for optical measurements. RBCs were separated and diluted in PBS for further processing. In order to observe and track RBCs with the optical system, a separate portion of RBCs was centrifuged and labeled with Rhodamine 6 G at a concentration of 10^{-3} M . Rhodamine 6 G is a fluorescent dye that can be adsorbed by the RBC membrane and also partially enters the RBC where it binds

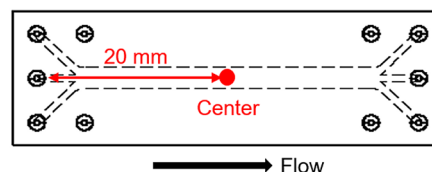


Fig. 3 Sketch of the straight microchannel used in this study, featuring a rectangular cross section with dimensions of $l \times w \times h = 40 \text{ mm} \times 2.33 \text{ mm} \times 150 \mu\text{m}$. The red point at the center indicates the measurement location

to the mitochondria of RBCs (Talib et al. 2019; Kutushov and Gorelik 2013). After labeling, RBCs were re-washed with PBS. By mixing 1.1 % labeled and 0.4 % non-labeled RBCs in PBS, a RBC suspension with concentration of 1.5 % was prepared for the measurements. The concentration of tracers (labeled RBCs) was specifically adjusted for A-PTV measurements. The total time from blood collection to the end of the experiments was always less than 24 h.

The suspension of spherical polymethyl methacrylate (PMMA) micro-particles, here referred to as pBAF, consists of a refractive index-matched (RIM) carrier liquid mixture and PMMA micro-particles. The RIM mixture contains 39.57 w% water and 60.43 w% ammonium thiocyanate to match the refractive index of PMMA particles ($n = 1.49$), thereby enhancing the optical accessibility of the suspension. The PMMA particles have a diameter of 7.5 μm . At 25 $^\circ\text{C}$, the density of PMMA particles in the pBAF is $\rho_p = 1190 \text{ kg/m}^3$, while the RIM mixture has a density of $\rho_f = 1134 \text{ kg/m}^3$, resulting in a relative density of $\rho_p/\rho_f = 1.05$. In comparison, at 36.5 $^\circ\text{C}$, the density of RBCs in the RBC suspension is $\rho_p = 1101 \text{ kg/m}^3$ (Kim et al. 1976), and the density of PBS is $\rho_f = 1004 \text{ kg/m}^3$ (Brown et al. 2011), resulting in a relative density of $\rho_p/\rho_f = 1.10$, as shown in Table 1. The pBAF contains a fixed volume fraction of 0.006 v% fluorescent PMMA particles serving as representative tracer particles while the remaining particles are transparent. Similar to the RBC suspension approach, this allows to change particle volume fractions while the particle image density of fluorescent tracers remains unaffected.

2.3 Experimental execution

Particle and velocity distributions are measured in both RBC suspension flows and pBAF flows to compare out-of-plane reconstruction errors of particle positions. To ensure a systematic comparison, particle volume fractions, relative densities between particles and fluid, as well as the bulk Reynolds number and particle Reynolds number, are matched between the two suspension systems, as shown in Table 1. Here, the bulk Reynolds number Re_b and the particle Reynolds number Re_p are defined as:

$$Re_b = \frac{\rho u_b D_h}{\eta}; \quad Re_p = Re_b \left(\frac{d_{\text{RBC}}}{h} \right)^2$$

Naturally, ρ and η denote the density and viscosity of the suspension, u_b is the bulk velocity of the suspension flow and D_h refers to the hydraulic diameter of the microchannel, which can be calculated by $D_h = 2hw/(h + w)$. The characteristic RBC diameter for the present measurements is $d_{\text{RBC}} = 7.5 \mu\text{m}$. The corresponding experimental parameters of both suspension systems are summarized in Table 1.

Prior to flow measurements, a calibration measurement is taken. The suspension is injected into the channel, and the flow is stopped to allow particles to settle to the channel bottom. After one hour, images are taken of sedimented particles in a scanning procedure. First the optical reference plane is aligned with the sedimented particles, such that its distance to the channel bottom can be assumed as one particle radius. The optical reference plane is defined to be the plane located midway between both focal planes of the optical system in astigmatic imaging. This location can be identified as particle images located in the reference plane are assumed to have an aspect ratio of one in the image plane. This first calibration step allows to identify the absolute position of the optical system with respect to the channel bottom. Next, a scanning procedure is performed. In the present study, the microchannel is translated in z -direction on a stage, while the optical system is fixed. By this, the reference plane is shifted in z -direction in pre-defined steps through the microchannel, thereby increasing the distance between optical reference plane and sedimented particles. This distance is referred to as relative out-of-plane position. At each scanning step, astigmatic images of sedimented particles are recorded. In this way, a correlation can be made between astigmatic particle images and known relative out-of-plane positions. Figure 6a shows exemplary RBC images at different relative out-of-plane positions. The optical axis is indicated with the z -coordinate. The scanning procedure is performed with a step size of 1 μm , which was determined through extensive testing to balance reconstruction accuracy and computational efficiency. Tests showed that reducing the step size further to 0.5 μm only improves out-of-plane reconstruction accuracy by approximately 1 %, while significantly increasing computational demand. A total of 200 raw images

Table 1 Composition, relative densities ρ_p/ρ_f , dynamic viscosities η , and matched bulk Reynolds number Re_b and particle Reynolds number Re_p of the suspension systems for experiments. RBC system

Acronym	Carrier Fluid	Volume Fraction Φ	ρ_p/ρ_f	η	Re_b	Re_p
RBC system	PBS buffer	1.5 v% RBC	1.10	0.78 mPas	150	0.38
pBAF system	RIM mixture	1.5 v% PMMA particle	1.05	1.98 mPas	150	0.38

denotes a RBC suspension diluted with PBS. pBAF system refers to a refractive index-matched carrier liquid mixture with PMMA micro-particles

are acquired for the calibration. In an actual measurement, only the reference plane position with respect to the channel bottom is known in advance, and the relative out-of-plane positions of suspended particles are reconstructed by comparing the astigmatic particle images from the measurement with those from the calibration using a 2D cross-correlation.

In the measurements, a pressure-driven RBC flow of 8.6 mL/min (corresponding to $Re_b = 150$) is generated. Measurements are taken at a constant temperature of 36.5 °C. The measurement volume for the RBC suspension is 550 μm in length and width, and 110 μm in depth. To ensure full coverage of the channel height, five equidistant reference planes were selected between 0 μm and 140 μm . A total of 1000 raw double-frame images were recorded during one experimental run, resulting in over $e4$ particle images for each evaluation. For pBAF measurements, the flow rate is adjusted to 19.5 ml/min to ensure Reynolds number similarity. Due to the different refractive index of the liquid the measurement volume depth covers 150 μm . Similarly, five equidistant reference planes were chosen, resulting in over $1.2e4$ particle images to be evaluated.

3 Data processing

To reconstruct the three-dimensional positions and velocities of RBCs in a flow by A-PTV, the astigmatism images need to go through a series of processing steps. First, the in-plane positions of the particle images are determined. Subsequently, the out-of-plane position is calculated for each particle image through a normalized cross-correlation procedure with a calibration image stack of known out-of-plane particle positions.

3.1 Image pre-processing and particle identification

For the identification of RBC or pBAF particle in-plane positions, recorded raw images must be pre-processed to enhance the signal-to-noise ratio (SNR). For this, stationary background noise and reflections are reduced through subtraction of a temporal mean image from each single image. To reduce salt-and-pepper noise, a sliding average filter of 5 pixel edge length is applied to all images including a Gaussian weighting function. A bandpass filter is then applied with a pass length in between 30 to 120 pixels. As particle image signals are within this frequency range, the noise level outside the bandpass width can be further reduced. This procedure has also been applied successfully for A-PTV in preceding studies (Brockmann and Hussong 2021; Brockmann et al. 2022; Blahout et al. 2020).

Furthermore, images are binarized using a global threshold. False object detections are deselected if either their pixel size is smaller than 600 pixels or their circularity is smaller than 0.3. Next, the centroids of the remaining particle images are evaluated to determine their in-plane positions. Based on these in-plane positions, image sections around individual particle images are cropped from the corresponding raw images for the reconstruction of out-of-plane position as described in the following. Both RBC and pBAF systems were processed identically to identify in-plane positions. Examples of single astigmatic RBC images are shown in Fig. 6a.

If multiple particle images are recorded at the same out-of-plane position during a calibration, a mean particle image is generated by averaging all individual particle images at that position to reduce the influence of particle-to-particle variations on the calibration. By this, the robustness of the evaluation procedure can be enhanced against deviations of individual particle images at the same out-of-plane position. The procedure is repeated for every reference plane, such that a stack of calibration images $I_c(i)$ with known relative out-of-plane positions $z = z_i$ between reference plane and particle position is obtained. Of course, relative out-of-plane positions are always a multiple of the stepping size interval δ_{step} of the depicted scanning procedure. An exemplary calibration subset for RBCs and spherical reference particles are shown in Fig. 4a, b.

3.2 Out-of-plane reconstruction

For calibration, Cierpka et al. (2011); Brockmann and Hussong (2021) applied a 2D Euclidean calibration procedure. However, as the labeling of RBCs generally results in low SNRs of recorded astigmatism images, a robust determination of the horizontal and vertical axes of astigmatic particle

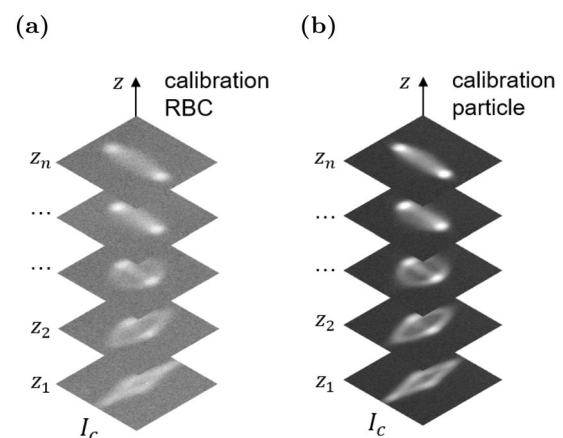


Fig. 4 Ensemble of a calibration image stack I_c of **a** RBC and **b** pBAF particle images

images turned out to be challenging. Therefore, a general defocusing particle tracking (GDPT) approach is chosen here according to Barnkob et al. (2015). In the present study, 1000 raw images are recorded at five measurement planes during the flow experiments to capture the entire 150 μm height of the microchannel. The five measurement planes are strategically selected to ensure that each height position is uniformly covered by two overlapping measurement volumes, enhancing accuracy and robustness in position determination. Cropped, individual particle images $I_m(j)$ of each measurement plane are subsequently correlated with each calibration image $I_c(i)$ identifying the best correlation match to identify the out-of-plane position $z = z_j$ of each particle in the measurement. The matching between the particle images $I_m(j)$ and the calibration image stack I_c is performed by calculating the normalized cross-correlation coefficient C , using the algorithm described by Lewis (1995). The maximum correlation coefficient between a pair of $I_m(j)$ and $I_c(i)$, referred to as C_m , which indicates the quality of the match between the two images. The resulting normalized cross-correlation coefficient C_m ranges between 0 and 1. A minimum threshold is defined for the cross-correlation coefficient, $C_m \geq 0.25$, to reduce outliers that may emanate from false positive particle images identifications or overlapping particle images. Ultimately, the three-dimensional coordinates of all identified RBCs in the experimental images are reconstructed.

Since all images are captured in a double-frame format, the three-dimensional velocity field can be further obtained by applying a nearest neighbor PTV algorithm, according to Tinevez (2024).

4 Effect of RBC orientation on out-of-plane reconstruction

Unlike the fluorescent spherical particles typically used as tracers for A-PTV measurements, RBCs are biconcave. As the rotation axis and angle may vary in a flow, the projected shape of an RBC changes. This effects the astigmatic particle image and in conclusion will have an effect on the out-of-plane reconstruction error. To evaluate the effect of RBC orientation on the out-of-plane reconstruction for A-PTV, a ray tracing approach is applied to synthetic, biconcave particles to generate astigmatic particle images. Here, the particle image generator developed by Rossi (2020) is utilized. First, a synthetic, biconcave particle is constructed recovering the typical shape of a RBC according to the mathematical expression from Pozrikidis (2003), as shown in Fig. 5a. It includes 30,000, uniformly distributed light point sources on the surface, assuming negligible transparency. To exclude the influence of noise, astigmatic biconcave particle images are

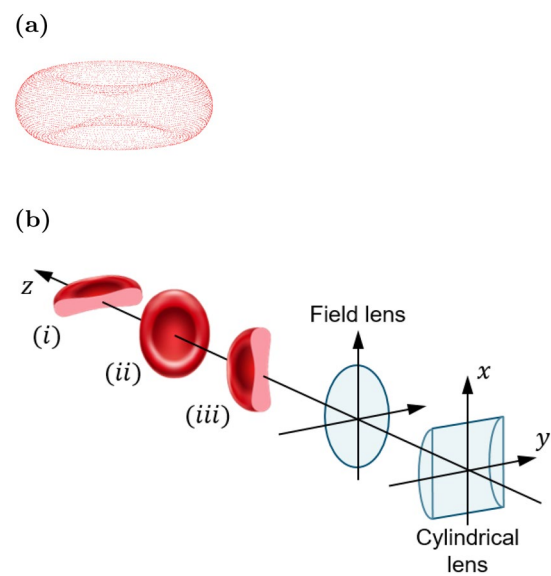


Fig. 5 **a** Biconcave RBC model with a diameter of 7.5 μm includes 30,000 uniformly distributed light point sources on the surface for ray-tracing simulations; **b** The lens configuration of the particle image generator and the three orientations of the RBC model: rotational symmetry axis parallel to (i) x-axis, (ii) z-axis and (iii) y-axis

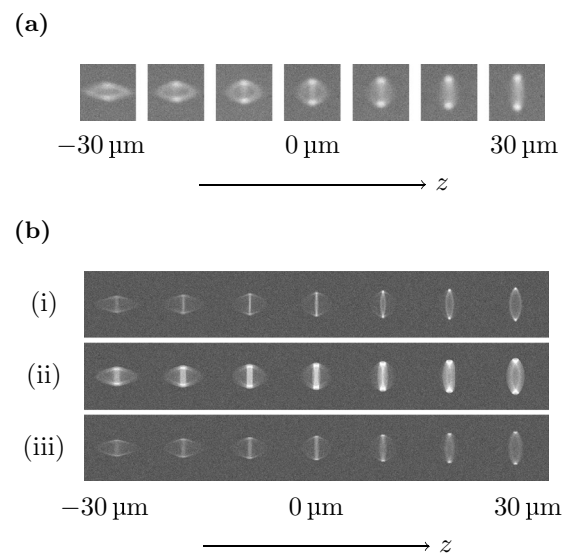


Fig. 6 **a** Representative images of labeled RBCs used for calibration at various out-of-plane coordinates ranging from $-30\ \mu\text{m}$ to $30\ \mu\text{m}$. **b** Synthetic astigmatic particle images for RBC with noise level ($\text{SNR} = 1.2$) generated by the ray-tracing image generator MicroSIG (Rossi 2020), with three orientations (i), (ii), (iii) corresponding to Fig. 5b. The horizontal axis represents the different z -coordinates during the scanning procedure

first generated without background noise, corresponding to $\text{SNR} = \infty$. Here, the SNR is defined as the ratio of the mean intensity of the astigmatic particle image in the region of interest to the mean intensity of the background

noise, according to Falchi and Romano (2009). Subsequently, images with SNR level ($\text{SNR} = 1.2$) matching those observed in actual RBC measurements are generated to compare and quantify the combined effects of orientation and background noise on the reconstruction accuracy. Moreover, the out-of-plane reconstruction accuracy for a synthetic, spherical particle (unaffected by orientation) is also quantified under both noise-free conditions and at an SNR level of $\text{SNR} = 1.2$, to analyze the effect of noise on the reconstruction accuracy. Further influences such as variations in labeling intensity are always excluded in the synthetic images.

The light is simulated to propagate along the z -axis, as illustrated in Fig. 5b. It passes a field lens with focal length $f = 350 \mu\text{m}$ and a cylindrical lens with a focal length of $f_{\text{cyl}} = 1000 \mu\text{m}$, ultimately projecting onto a synthetic image plane where an astigmatic image is created. It may be noted that the image generator code uses a highly simplified optical model, its optical parameters do not resemble all optical features of the experimental setup. Therefore, depicted focal lengths are found by an iterative process in which a best possible matching between synthetic particle images and those of the experiments was achieved with a maximum correlation coefficient $C_m > 0.85$ between them under conditions with background noise. Astigmatic images are generated for three different orientations with respect to the image plane as illustrated in Fig. 5b. They represent three extreme cases of orientation. The synthetic particle images were generated with a step size of $\delta_{\text{step}} = 1 \mu\text{m}$. Examples of the resulting synthetic particle images at different defocus positions are displayed in Fig. 6b.

It can be observed that under orientation (ii), where the RBC's maximum projection area is perpendicular to the z -axis, the overall image brightness is higher compared to orientations (i), and (iii). As the z -coordinate increases, RBCs of different orientations exhibit similar image shape

changes. By evaluating the cross-correlation coefficients among particle images of those three orientations, it is possible to gain an estimate of the out-of-plane reconstruction error. This is done by evaluating synthetic particle images with the same A-PTV code that is also used for experimental evaluations. For this, each particle image of one z -position is cross-correlated with each particle image of another orientation.

Similar to the calibration procedure, particle images under orientation (ii) as shown in Fig. 6b are set as calibration image stack, as these particles have a typical orientation as sedimented calibration particles in the experiment. Particle images under the two other depicted orientations (i) and (iii) were cross-correlated with the calibration particle images of orientation (ii). When the distance between optical reference plane and a particle of unknown z -position is identical to that of a calibration particle with a known z -coordinate z_{ref} , i.e., when reconstructed z -coordinate $z_{\text{meas}} = z_{\text{ref}}$, the resulting astigmatic images are expected to be highly similar. This similarity leads to the highest correlation and maximum correlation coefficients C_m . The reconstructed out-of-plane coordinates z_{meas} of particles and corresponding maximum correlation coefficients C_m are indicated in Fig. 7 by blue and red markers, respectively. The x -axis represents the reference z -coordinates.

A perfect match between the reference z -coordinate and the reconstructed z -coordinate is derived when data points fall onto the black bisection curve. Figure 7a, b indicates results without background noise ($\text{SNR} = \infty$), and Fig. 7c, d includes a noise levels equivalent to real RBC measurements ($\text{SNR} = 1.2$). The reconstructed z -coordinates and maximum correlation coefficients C_m are plotted for orientation (i) in Fig. 7a, c, and for orientation (iii) in Fig. 7b, d. As seen in Fig. 7a, b as well as Fig. 7c, d, the reconstructed z -coordinates and the maximum correlation coefficients C_m

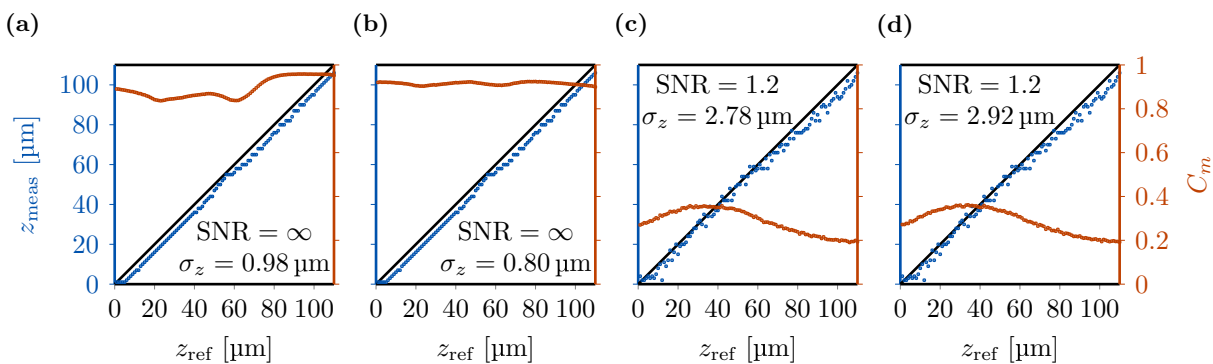


Fig. 7 Assessment of orientation effects on reconstruction accuracy using synthetic images under two noise conditions: **a, b** no noise ($\text{SNR} = \infty$) and **c, d** noise levels equivalent to real RBC measurements ($\text{SNR} = 1.2$). The reconstructed z -coordinate z_{meas} and maxi-

imum correlation coefficients C_m are plotted for different orientations (i) to (ii) in **(a)**, **(c)**, and (iii) to (ii) in **(b)**, **(d)**, respectively. The calibration step size is $\delta_{\text{step}} = 1 \mu\text{m}$

for both orientations (i) and (iii) are very similar. In Fig. 7a, b, the reconstructed z -coordinates show a shift of approximately $4\ \mu\text{m}$ toward lower values and are thus located below the black diagonal reference curve. This underestimation of RBC z -coordinates for orientations (i) and (iii) may occur as the RBC side that is facing toward the lens system is closer to the camera by one particle radius. This systematic error becomes less apparent in Fig. 7c, d due to a background noise induced, higher random error. Furthermore, the correlation coefficient C_m significantly decreases from ≈ 0.8 in Fig. 7a, b to ≈ 0.3 in Fig. 7c, d by adding noise (SNR = 1.2).

The deviation in the reconstructed z -coordinate from the perfect match is evaluated in terms of absolute out-of-plane reconstruction error σ_z and relative out-of-plane reconstruction error ε_z in z -direction. The latter is normalized with the depth of measurement volume H_{meas} :

$$\sigma_z = \sqrt{\frac{1}{N-1} \sum_{i=1}^N [\Delta z(i) - \widehat{\Delta z}(i)]^2} \tag{1}$$

$$\varepsilon_z = \frac{\sigma_z}{H_{meas}} \tag{2}$$

with $\Delta z(i) = z_{meas}(i) - z_{ref}(i)$.

where N is the number of evaluated particle images, $z_{meas}(i)$ is the reconstructed z -coordinate, $z_{ref}(i)$ is the reference coordinate and i is the index of evaluated particle images. For the ray-tracing simulation $H_{meas} = 110\ \mu\text{m}$.

The absolute out-of-plane reconstruction errors evaluated with biconcave and spherical synthetic particle images under different noise conditions are summarized in Table 2. Synthetic images without background noise result in a low absolute out-of-plane reconstruction error, with values of $\sigma_z = 0.98\ \mu\text{m}$ and $\sigma_z = 0.81\ \mu\text{m}$ for orientations (i) and (iii), respectively. The corresponding relative out-of-plane reconstruction errors are $\varepsilon_z = 0.009$ and $\varepsilon_z = 0.007$. In contrast, the absolute out-of-plane reconstruction error increases to $\approx 3\ \mu\text{m}$ for synthetic images with a SNR level of real RBC

Table 2 Comparison of absolute out-of-plane reconstruction errors evaluated with synthetic images of spherical and biconcave particles that resemble the shape of RBCs under two noise conditions: no noise (SNR = ∞) and noise levels equivalent to real RBC measurements (SNR = 1.2)

Particle Shape	Orientation	SNR = ∞	SNR = 1.2
Spherical	–	$\sigma_z = 0.00\ \mu\text{m}$	$\sigma_z = 1.51\ \mu\text{m}$
Biconcave (RBC)	(i)	$\sigma_z = 0.98\ \mu\text{m}$	$\sigma_z = 2.78\ \mu\text{m}$
Biconcave (RBC)	(iii)	$\sigma_z = 0.80\ \mu\text{m}$	$\sigma_z = 2.92\ \mu\text{m}$

measurements (SNR = 1.2). In comparison, the absolute out-of-plane reconstruction error of synthetic, spherical particles increases from 0 to $1.51\ \mu\text{m}$ for SNR = 1.2. Consequently, both background noise and RBC orientation have an influence on the out-of-plane reconstruction error.

It may be noted that synthetic particle images were created, assuming that only the particle surface emits fluorescent signal. Furthermore, it is assumed that the particle labeling intensity is the same for all particles.

To prove the feasibility of A-PTV measurements taken on RBCs, experimental errors of out-of-plane particle position and particle velocities are determined. In contrast to synthetic image analysis, the effects of background noise and variations in labeling intensity are inherently considered in the experiments. Results of a RBC and a pBAF suspension flow are compared. The pBAF system was chosen for comparison as it is representative for a typical particle system suitable for A-PTV due to its good optical accessibility and high SNR.

5 Experimental reconstruction of the out-of-plane position error

To obtain the out-of-plane position error for RBCs and spherical particles experimentally, two scanning procedures are performed for each particle group on sedimented particles using a scanning step size of $\delta_{step} = 1\ \mu\text{m}$. The first scanning stack is used to create a stack of astigmatic calibration images of known out-of-plane position as described before. Then, the out-of-plane position of each single particle of the second scanning set is determined applying the cross-correlation-based evaluation code. As for sedimented particles, the actual out-of-plane particle positions in the second scanning stack are also known, the reconstructed and actual out-of-plane positions can then be compared to evaluate the reconstruction accuracy. For the RBCs and pBAF systems, a total number of $e4$ and $1.2e4$ particle images were evaluated, respectively. The number of particle images for the RBC sample is smaller compared to that of fluorescent particles due to varying labeling quality and higher background noise, which cause some astigmatic images of RBCs to be unclear and subsequently excluded by the algorithm.

Figure 8a, b shows in blue the reconstructed out-of-plane positions z_{meas} and in red corresponding, maximum normalized cross-correlation coefficients C_m as function of the actual out-of-plane positions for both RBCs and pBAF, respectively.

As out-of-plane reconstruction is based on a cross-correlation procedure, the corresponding correlation coefficient values can be analyzed. They are a qualitative indicator

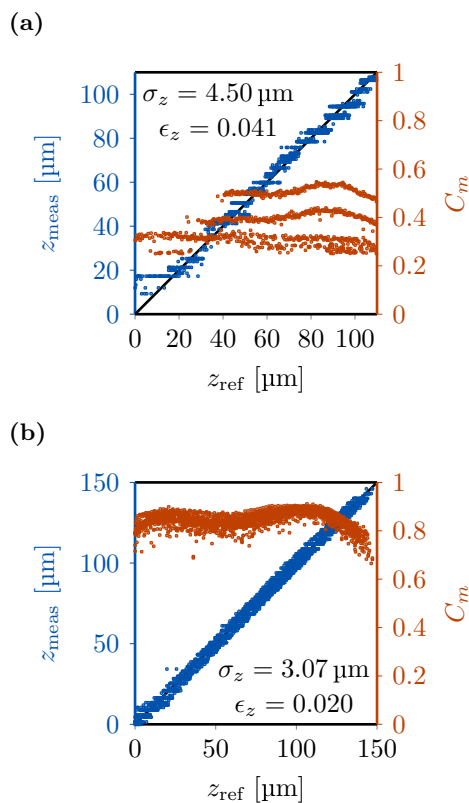


Fig. 8 Reconstructed out-of-plane positions z_{meas} and the corresponding maximum normalized cross-correlation coefficients C_m with the known reference positions z_{ref} for **a** RBC and **b** pBAF

for the similarity of particle images. For RBCs particles, maximum normalized cross-correlation coefficients vary between 0.25 and 0.55 while correlation coefficients for pBAF are significantly higher ranging between 0.7 and 0.9, as shown in Fig. 8a, b. The three parallel lines observed in the results correspond to three individual particles with varying labeling quality in the test images. These lines do not indicate distinct particle classes but instead reflect natural variations in particle labeling quality. Increasing the size of the testing ensemble would likely result in a more continuous distribution within this range. Overall, lower correlations coefficients are an indication for a lower SNR level in the RBC images compared to those in the pBAF system. On the other hand, a huge spread in correlation coefficients of the RBC measurements indicate larger particle image variations between individual RBCs. The variation in fluorescence signal intensities originate from variations in fluorescent molecule uptake by the RBCs themselves.

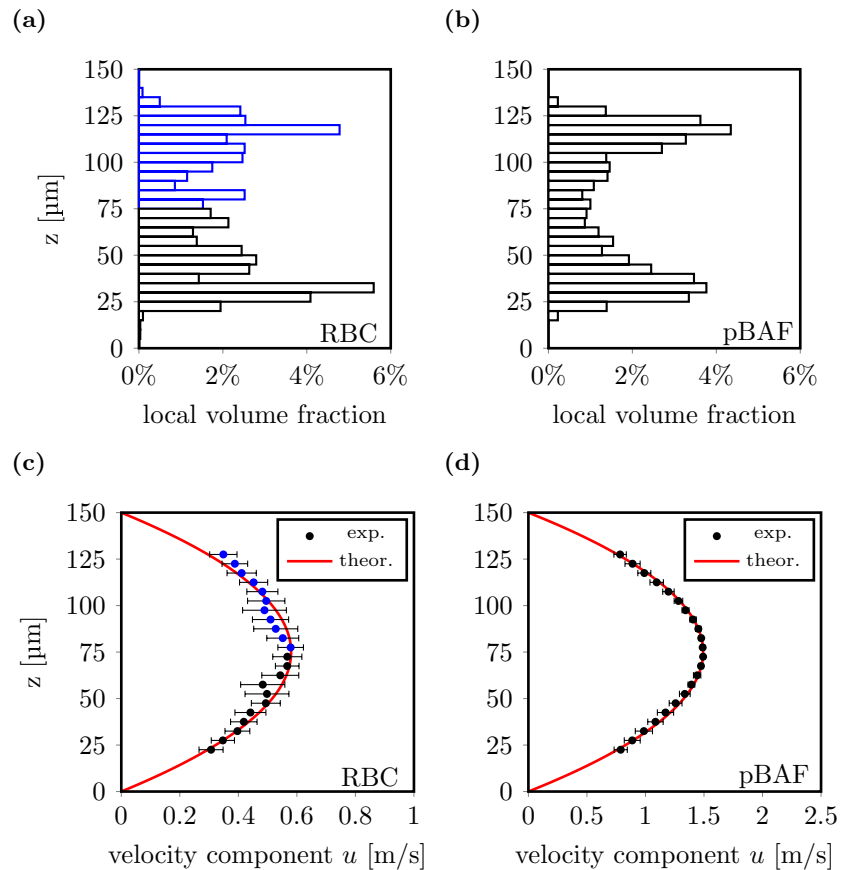
As mentioned before, the relative out-of-plane reconstruction error ϵ_z is normalized with the total depth of the corresponding measurement volume H_{meas} , defined by

Eq. 2. For the RBC system a measurement volume depth of $H_{\text{meas}} = 110 \mu\text{m}$ is realized while for the pBAF system it covers $H_{\text{meas}} = 150 \mu\text{m}$. From the measurement results displayed in Fig. 8, absolute and relative out-of-plane reconstruction errors were determined for the RBC suspension to $\sigma_z = 4.50 \mu\text{m}$ and $\epsilon_z = 0.041$, while for the pBAF system the errors read $\sigma_z = 3.07 \mu\text{m}$ and $\epsilon_z = 0.020$. Overall, RBC measurements result in larger reconstruction errors as the SNR is significantly lower and particle images variations are larger due to, e.g., labeling or shape variations. Especially reduced SNRs may lead to a loss of astigmatic image information where the particle image intensity lowers to the background noise level.

6 Particle distribution

Measurements of the particle and velocity distributions over the channel height are determined on the symmetry axis of the channel as indicated in Fig. 3. As discussed in section 2.1, the width of the channel is significantly larger than its height; therefore, the flow can be approximated as a two-dimensional plane Poiseuille flow. Additionally, in streamwise direction no changes in velocity or particle distribution are expected over the length of the measurement volume. Therefore, results in spanwise and streamwise direction can be averaged, resulting in mean velocity and concentration profiles over the channel height. Resulting particle distributions of the RBC and pBAF suspension flow are shown in Fig. 9a, b for $Re_b = 150$ and a mean volume fraction of $\Phi = 1.5\%$. The results are presented as histograms with a bin width of $\Delta h = 5 \mu\text{m}$, which has been adapted to the out-of-plane reconstruction error. The local volume fraction is determined by calculating the ratio of the number of particles within each bin and normalizing it with the total number of particles. Assuming that the overall particle number corresponds to the known average volume fraction, local volume fractions are deduced at each bin. This is a fair assumption as firstly, no particle losses due to sedimentation or sticking could be observed during the experiments due to small relative densities and short residence times of particles in the fluidic system. Secondly, both suspension systems are at low volume fraction in a narrow flow geometry and are therefore optically well accessible. Especially the pBAF system provides full optical accessibility is provided while the optical accessibility in the RBC system is slightly reduced. Therefore, the RBC concentration distribution was evaluated only to half the channel height with an inverted microscope and subsequently repeated with an upright system under identical experimental conditions and the same RBC suspension (here indicated with blue bars in Fig. 9a. Furthermore, it

Fig. 9 Distribution of the local volume fraction of identified labeled particles within the measurement volume for flow at $Re_b = 150$, for the **a** RBC and **b** pBAF system. The primary velocity component magnitude, calculated using the PTV algorithm, is shown alongside with the theoretical Hagen-Poiseuille velocity profile for the **c** RBC and **d** pBAF system. Blue data points represent complementary measurements using an upright system under identical experimental conditions and the same RBC suspension



was tested that the varying shapes of astigmatic particle images induced by different out-of-plane positions have minimal impact on the detection probability of the algorithm. This effect introduces a potential relative deviation in the local particle volume fraction of less than 7 % at a 95 % confidence level.

Figure 9a, b shows that both particle systems are subject to inertial particle migration. This is to be expected as $Re_p = 0.38$ and migration effects are known to play a role if the particle Reynolds number reaches an order of magnitude of $\mathcal{O}(10^{-1})$ (Bhagat et al. 2009). While the RBC concentration distributions shows stronger local variations that originate from a larger data spread and smaller amount of evaluated particle images, the overall trend between both particle systems is very similar. In both particle systems, a particle depleted area forms near the wall due to wall-lift forces, known as cell-free layer (CFL) for blood flows. Furthermore, a characteristic pseudo-Segré–Silberberg annulus (PSSA) can be identified at z -positions of approximately $z = 35 \mu\text{m}$ and $z = 115 \mu\text{m}$. For dilute suspension flows of neutrally buoyant particles, the PSSA results from a force balance of two inertial migration forces that dominate lateral particle migration in the absence of acceleration and curved stream lines (Zhang et al. 2017; Amini et al. 2014). These forces are

the wall-lift force, which directs particles away from the channel walls, and the shear-gradient force, which directs particles from the channel center toward the walls. At a certain off-center position, these forces balance, resulting in the formation of the PSSA (Segré and Silberberg 1962). Overall, the similarity in RBC and pBAF concentration distributions for particle concentrations of $\Phi = 1.5 \%$ at $Re_b = 150$ indicate that the migration dynamics without streamline curvature or acceleration for elastic and deformable RBCs can be very similar compared to that of spherical, stiff particles as in the pBAF system.

Velocity profiles can be derived from the same measurements as double-frame images have been recorded throughout. A number of 3900 and 3000 particle image pairs have been evaluated by means of A-PTV for the RBC and pBAF systems, shown in Fig. 9c, d, respectively. The red curve represents the theoretical Poiseuille flow profile for a constant suspension viscosity (see Table 1) at the same volumetric flow rate. Overall, a good match between particle velocities and the theoretical curve of a one-phase flow can be observed. For the pBAF system, the mean standard deviation of velocity measurements equals $\sigma_u = 0.04 \text{ m/s}$, while for the RBC system, the value only slightly increases to 0.06 m/s . Since the flow velocities are calculated based on the displacement of particles captured in double-frame

images, and assuming the laser's double-frame time interval is sufficiently precise, the corresponding in-plane position uncertainties in the flow direction can be estimated as approximately $1.2\ \mu\text{m}$ for the pBAF system and $3.0\ \mu\text{m}$ for the RBC system.

7 Conclusion

The present work investigates the capability of A-PTV to measure the 3D red blood cell migrations dynamics for technically relevant flow geometries and Reynolds numbers. For this, a systematic study of reconstruction errors was done for the first time based on synthetic and experimental data where fluorescently labeled RBCs were used as tracers.

For the evaluation of 3D RBC positions in a flow, the role of the particle orientation on the out-of-plane reconstruction accuracy must be evaluated. Also, lower SNR levels in the measurement data may effect measurement errors. These error sources are analyzed using synthetic particle images of RBCs and spherical particles with different orientations and noise levels. Furthermore, the out-of-plane reconstruction error of the RBC systems is experimentally compared to the pBAF system to evaluate the lumped effect of reduced SNR, reduced particle labeling intensity and homogeneity, as well as reduced optical accessibility of the RBC system. For this, the A-PTV technique is applied to an RBC suspension flow with a volume fraction of $\Phi = 1.5\%$ and a bulk Reynolds number of $Re_b = 150$ in a rectangular microchannel, tracking the RBC concentration and velocity distributions. The results indicate that the absolute out-of-plane reconstruction error in the red blood cell suspension system equals $\sigma_z = 3.07\ \mu\text{m}$ which is approximately twice as large as that of the refractive index-matched system.

In general, the concentration distributions obtained for the RBC and the pBAF systems show similar trends. The velocity profiles for both systems align well with the theoretical Hagen-Poiseuille profile, indicating that local variations in effective viscosity that may be caused by local particle concentrations do not significantly impact the flow field at given bulk concentration of 1.5% .

In this study a volume fraction of 1.5% is selected to ensure sufficient optical accessibility for the A-PTV technique. This represents the first step in directly using fluorescently labeled RBCs as tracers for 3D RBC migration dynamics measurements. It is acknowledged, however, that this volume fraction is substantially lower than physiological hematocrit levels (approximately 40%). At higher volume fractions, increased interactions between RBCs would result in more complex rheological behavior, potentially deviating from the dilute suspension dynamics observed in this study.

Additionally, the study employs a washed fluid system with PBS as the carrier fluid instead of plasma. This washing process removes proteins and other components that could influence certain phenomena, such as Rouleaux formation, potentially causing the rheological behavior of the studied RBC suspension to deviate further from that of real blood. Furthermore, achieving optical accessibility in denser suspensions remains a challenge, as labeled RBCs may only be observed in the first few layers near the CFL. Extending this technique to higher volume fractions may require additional measures, such as the use of optically transparent ghost cells (hemoglobin-depleted RBCs), to maintain sufficient optical clarity.

Analysis of astigmatic particle images of synthetic surface-labeled, biconcave-shaped RBC particles showed that different particle orientations can introduce out-of-plane reconstruction errors of approximately $1\ \mu\text{m}$. The small error can be attributed to the fact that the characteristic features of the astigmatic particle image are hardly affected by the RBC orientation, while the overall intensity of the particle image varies with orientation. In addition, the effect of background noise on the reconstruction accuracy is investigated using synthetic images with different signal-to-noise ratios. For experimentally relevant SNRs, the reconstruction error of synthetic images increases to approximately $3\ \mu\text{m}$ when being combined with different RBC orientations. Experimentally determined reconstruction errors are larger, e.g., due to inhomogeneous labeling. For a calibration step size of $\delta_{\text{step}} = 1\ \mu\text{m}$, experimentally determined out-of-plane reconstruction errors were found to be $\sigma_z = 4.50\ \mu\text{m}$ for the RBC suspension and $\sigma_z = 3.07\ \mu\text{m}$ for the pBAF system.

Overall, the present work demonstrates the capability of A-PTV to measure the 3D red blood cell migrations dynamics for technically relevant flow geometries and Reynolds numbers providing for the first time a systematic study of particle orientation and SNR induced reconstruction errors.

Acknowledgements Not applicable.

Author contributions A. S. contributed to conceptualization, methodology, investigation, experiments, data interpretation, and drafting the manuscript. T. W. assisted in the experiments and contributed to the manuscript review and editing. F. K., F. W. and T. B. provided support and scientific guidance for blood-related experiments and contributed to the manuscript review. J. H. supervised the conceptualization, methodology and data interpretation, and contributed to manuscript review and editing.

Funding Open Access funding enabled and organized by Projekt DEAL. This research was funded by the German Research Foundation (DFG) under grant number HU 2264/14-1 and the Hessian research funding program LOEWE (research cluster FLOW FOR LIFE), grant number LOEWE/2/14/519/03/07.001(0002)/78.

Data availability Data are available from authors upon request.

Declarations

Conflict of interest The authors declare no conflict of interest related to this work.

Open Access This article is licensed under a Creative Commons Attribution 4.0 International License, which permits use, sharing, adaptation, distribution and reproduction in any medium or format, as long as you give appropriate credit to the original author(s) and the source, provide a link to the Creative Commons licence, and indicate if changes were made. The images or other third party material in this article are included in the article's Creative Commons licence, unless indicated otherwise in a credit line to the material. If material is not included in the article's Creative Commons licence and your intended use is not permitted by statutory regulation or exceeds the permitted use, you will need to obtain permission directly from the copyright holder. To view a copy of this licence, visit <http://creativecommons.org/licenses/by/4.0/>.

References

- Amini H, Lee W, Di Carlo D (2014) Inertial microfluidic physics. *Lab Chip* 14(15):2739–2761. <https://doi.org/10.1039/c4lc00128a>
- Brown PH, Balbo A, Zhao H, Ebel C, Schuck P (2011) Density contrast sedimentation velocity for the determination of protein partial-specific volumes. *PLoS ONE* 6(10):26221. <https://doi.org/10.1371/journal.pone.0026221>
- Bugliarello G, Hayden JW (1963) Detailed characteristics of the flow of blood in vitro. *Transactions of the Society of Rheology* 7(1):209–230. <https://doi.org/10.1122/1.548964>
- Brockmann P, Hussong J (2021) On the calibration of astigmatism particle tracking velocimetry for suspensions of different volume fractions. *Experiments in Fluids* 62(1) <https://doi.org/10.1007/s00348-020-03120-4>
- Bhagat AAS, Kuntaegowdanahalli SS, Papautsky I (2009) Inertial microfluidics for continuous particle filtration and extraction. *Microfluid Nanofluid* 7(2):217–226. <https://doi.org/10.1007/s10404-008-0377-2>
- Barnkob R, Kähler CJ, Rossi M (2015) General defocusing particle tracking. *Lab Chip* 15(17):3556–3560. <https://doi.org/10.1039/c5lc00562k>
- Blahout S, Reinecke SR, Tabaei Kazerooni H, Kruggel-Emden H, Hussong J (2020) On the 3d distribution and size fractionation of microparticles in a serpentine microchannel. *Microfluidics and Nanofluidics* 24(3) <https://doi.org/10.1007/s10404-020-2326-7>
- Brockmann P, Symanczyk C, Ennayar H, Hussong J (2022) Utilizing aptv to investigate the dynamics of polydisperse suspension flows beyond the dilute regime. *Experiments in Fluids* 63(8) <https://doi.org/10.1007/s00348-022-03464-z>
- Chen S, Angarita-Jaimes N, Angarita-Jaimes D, Pelc B, Greenaway AH, Towers CE, Lin D, Towers DP (2009) Wavefront sensing for three-component three-dimensional flow velocimetry in microfluidics. *Exp Fluids* 47(4–5):849–863. <https://doi.org/10.1007/s00348-009-0737-z>
- Choi Y-S, Lee S-J (2010) Holographic analysis of three-dimensional inertial migration of spherical particles in micro-scale pipe flow. *Microfluid Nanofluid* 9(4–5):819–829. <https://doi.org/10.1007/s10404-010-0601-8>
- Coutinho G, Moita AS, Rossi M, Moreira ALN (2023) Experimental perspective on the mechanisms for near-wall accumulation of platelet-size particles in pressure-driven red blood cell suspension flows. *Physical Review Fluids* 8(10) <https://doi.org/10.1103/PhysRevFluids.8.103101>
- Cierpka C, Rossi M, Segura R, Kähler CJ (2011) On the calibration of astigmatism particle tracking velocimetry for microflows. *Meas Sci Technol* 22(1):015401. <https://doi.org/10.1088/0957-0233/22/1/015401>
- Cierpka C, Segura R, Hain R, Kähler CJ (2010) A simple single camera 3c3d velocity measurement technique without errors due to depth of correlation and spatial averaging for microfluidics. *Meas Sci Technol* 21(4):045401. <https://doi.org/10.1088/0957-0233/21/4/045401>
- Discetti S, Coletti F (2018) Volumetric velocimetry for fluid flows. *Meas Sci Technol* 29(4):042001. <https://doi.org/10.1088/1361-6501/aaa571>
- Fåhræus R, Lindqvist T (1931) The viscosity of the blood in narrow capillary tubes. *Am J Physiol* 96(3):562–568. <https://doi.org/10.1152/ajplegacy.1931.96.3.562>
- Falchi M, Romano GP (2009) Evaluation of the performance of high-speed piv compared to standard piv in a turbulent jet. *Exp Fluids* 47(3):509–526. <https://doi.org/10.1007/s00348-009-0682-x>
- Fraser KH, Zhang T, Taskin ME, Griffith BP, Wu ZJ (2012) A quantitative comparison of mechanical blood damage parameters in rotary ventricular assist devices: shear stress, exposure time and hemolysis index. *J Biomech Eng* 134(8):081002. <https://doi.org/10.1115/1.4007092>
- Japee SA, Pittman RN, Ellis CG (2005) Automated method for tracking individual red blood cells within capillaries to compute velocity and oxygen saturation. *Microcirculation* (New York, N.Y. : 1994) 12(6), 507–515 <https://doi.org/10.1080/10739680591003341>
- Kutushov M, Gorelik O (2013) Low concentrations of rhodamine-6g selectively destroy tumor cells and improve survival of melanoma transplanted mice. *Neoplasma* 60(3):262–273. https://doi.org/10.4149/neo_2013_035
- Kim S, Kong RL, Popel AS, Intaglietta M, Johnson PC (2006) A computer-based method for determination of the cell-free layer width in microcirculation. *Microcirculation* (New York, N.Y. : 1994) 13(3), 199–207 <https://doi.org/10.1080/10739680600556878>
- Kim HD, Luthra MG, Hildenbrandt GR, Zeidler RB (1976) Pig reticulocytes: II. characterization of density-fractionated maturing reticulocytes. *The American journal of physiology* 230(6), 1676–1682 <https://doi.org/10.1152/ajplegacy.1976.230.6.1676>
- Knüppel F, Malchow S, Sun A, Hussong J, Hartmann A, Wurm F-H, Torner B (2024) Viscosity modeling for blood and blood analog fluids in narrow gap and high reynolds numbers flows. *Micromachines* 15(6) <https://doi.org/10.3390/mi15060793>
- Knüppel F, Sun A, Wurm F-H, Hussong J, Torner B (2023a) Effect of particle migration on the stress field in microfluidic flows of blood analog fluids at high reynolds numbers. *Micromachines* 14(8) <https://doi.org/10.3390/mi14081494>
- Knüppel F, Thomas I, Wurm F-H, Torner B (2023b) Suitability of different blood-analogous fluids in determining the pump characteristics of a ventricular assist device. *Fluids* 8(5) <https://doi.org/10.3390/fluids8050151>
- Kao HP, Verkman AS (1994) Tracking of single fluorescent particles in three dimensions: use of cylindrical optics to encode particle position. *Biophys J* 67(3):1291–1300. [https://doi.org/10.1016/S0006-3495\(94\)80601-0](https://doi.org/10.1016/S0006-3495(94)80601-0)
- Lewis JP (1995) Fast normalized cross-correlation. In: *Vision. Interface* 10:120–123
- Lima R, Ishikawa T, Imai Y, Takeda M, Wada S, Yamaguchi T (2009) Measurement of individual red blood cell motions under high hematocrit conditions using a confocal micro-ptv system. *Ann Biomed Eng* 37(8):1546–1559. <https://doi.org/10.1007/s10439-009-9732-z>
- Lima R, Wada S, Takeda M, Tsubota K-I, Yamaguchi T (2007) In vitro confocal micro-piv measurements of blood flow in a square micro-channel: the effect of the haematocrit on instantaneous velocity

- profiles. *J Biomech* 40(12):2752–2757. <https://doi.org/10.1016/j.jbiomech.2007.01.012>
- Lima R, Wada S, Tanaka S, Takeda M, Ishikawa T, Tsubota K-I, Imai Y, Yamaguchi T (2008) In vitro blood flow in a rectangular pdms microchannel: experimental observations using a confocal micro-piv system. *Biomed Microdevice* 10(2):153–167. <https://doi.org/10.1007/s10544-007-9121-z>
- Lima R, Wada S, Tsubota K-I, Yamaguchi T (2006) Confocal micro-piv measurements of three-dimensional profiles of cell suspension flow in a square microchannel. *Meas Sci Technol* 17(4):797–808. <https://doi.org/10.1088/0957-0233/17/4/026>
- Park JS, Choi CK, D. Kihm K (2004) Optically sliced micro-piv using confocal laser scanning microscopy (clsm). *Experiments in Fluids* 37(1), 105–119 <https://doi.org/10.1007/s00348-004-0790-6>
- Peterson SD, Chuang H-S, Wereley ST (2008) Three-dimensional particle tracking using micro-particle image velocimetry hardware. *Meas Sci Technol* 19(11):115406. <https://doi.org/10.1088/0957-0233/19/11/115406>
- Pozrikidis C (2003) Numerical simulation of the flow-induced deformation of red blood cells. *Ann Biomed Eng* 31(10):1194–1205. <https://doi.org/10.1114/1.1617985>
- Rodrigues RO, Lopes R, Pinho D, Pereira AI, Garcia V, Gassmann S, Sousa PC, Lima R (2016) In vitro blood flow and cell-free layer in hyperbolic microchannels: Visualizations and measurements. *BioChip J* 10(1):9–15. <https://doi.org/10.1007/s13206-016-0102-2>
- Rossi M, Marin A, Cevheri N, Kähler CJ, Yoda M (2019) Particle distribution and velocity in electrokinetically induced banding. *Microfluidics and Nanofluidics* 23(5) <https://doi.org/10.1007/s10404-019-2227-9>
- Rossi M (2020) Synthetic image generator for defocusing and astigmatic piv/ptv. *Meas Sci Technol* 31(1):017003. <https://doi.org/10.1088/1361-6501/ab42bb>
- Ravichandran AK, Parker J, Novak E, Joseph SM, Schilling JD, Ewald GA, Silvestry S (2014) Hemolysis in left ventricular assist device: a retrospective analysis of outcomes. *J Heart Lung Transplant* 33(1):44–50. <https://doi.org/10.1016/j.healun.2013.08.019>
- Speidel M, Jonás A, Florin E-L (2003) Three-dimensional tracking of fluorescent nanoparticles with subnanometer precision by use of off-focus imaging. *Opt Lett* 28(2):69–71. <https://doi.org/10.1364/ol.28.000069>
- Satake S-I, Kunugi T, Sato K, Ito T, Taniguchi J (2005) Three-dimensional flow tracking in a micro channel with high time resolution using micro digital-holographic particle-tracking velocimetry. *Opt Rev* 12(6):442–444. <https://doi.org/10.1007/s10043-005-0442-y>
- Satake S-I, Kunugi T, Sato K, Ito T, Kanamori H, Taniguchi J (2006) Measurements of 3d flow in a micro-pipe via micro digital holographic particle tracking velocimetry. *Meas Sci Technol* 17(7):1647–1651. <https://doi.org/10.1088/0957-0233/17/7/002>
- Segré G, Silberberg A (1962) Behaviour of macroscopic rigid spheres in poiseuille flow part 2. experimental results and interpretation. *Journal of Fluid Mechanics* 14(1), 136–157 <https://doi.org/10.1017/S0022112062001111>
- Talib AJ, Fisher A, Voronine DV, Sinyukov AM, Bustamante Lopez SC, Ambardar S, Meissner KE, Scully MO, Sokolov AV (2019) Fluorescence imaging of stained red blood cells with simultaneous resonance raman photostability analysis. *Analyst* 144(14):4362–4370. <https://doi.org/10.1039/c9an00757a>
- Tinevez J (2024) Nearest-neighbor Linker, 1.1.0.0, MATLAB Central File Exchange (2024). Retrieved September 18, . <https://www.mathworks.com/matlabcentral/fileexchange/33772-nearest-neighbor-linker>
- Tangelder GJ, Slaaf DW, Muijtjens AM, Arts T, oude Egbrink MG, Reneman RS (1986) Velocity profiles of blood platelets and red blood cells flowing in arterioles of the rabbit mesentery. *Circulation research* 59(5), 505–514 <https://doi.org/10.1161/01.res.59.5.505>
- Williams SJ, Park C, Wereley ST (2010) Advances and applications on microfluidic velocimetry techniques. *Microfluid Nanofluid* 8(6):709–726. <https://doi.org/10.1007/s10404-010-0588-1>
- Yu H, Engel S, Janiga G, Thévenin D (2017) A review of hemolysis prediction models for computational fluid dynamics. *Artif Organs* 41(7):603–621. <https://doi.org/10.1111/aor.12871>
- Zhang J, Li W, Alici G (2017) Inertial microfluidics: Mechanisms and applications. In: Zhang, D., Wei, B. (eds.) *Advanced Mechatronics and MEMS Devices II*. Microsystems and Nanosystems, pp. 563–593. Springer International Publishing, Cham . https://doi.org/10.1007/978-3-319-32180-6_25

Publisher's Note Springer Nature remains neutral with regard to jurisdictional claims in published maps and institutional affiliations.

Authors and Affiliations

Ang Sun¹ · Till Werner¹ · Finn Knüppel² · Frank-Hendrik Wurm² · Benjamin Torner² · Jeanette Hussong¹

✉ Jeanette Hussong
hussong@sla.tu-darmstadt.de

Ang Sun
sun@sla.tu-darmstadt.com

Till Werner
werner@sla.tu-darmstadt.de

Finn Knüppel
finn.knueppel@uni-rostock.de

Frank-Hendrik Wurm
hendrik.wurm@uni-rostock.de

Benjamin Torner
benjamin.torner@uni-rostock.de

¹ Institute for Fluid Mechanics and Aerodynamics, Technical University of Darmstadt, Peter-Grünberg-Straße 10, 64287 Darmstadt, Hessen, Germany

² Institute of Turbomachinery, Faculty for Mechanical Engineering and Ship Design, University of Rostock, Albert-Einstein-Straße 2, 18059 Rostock, Mecklenburg-Vorpommern, Germany